New Journal of Physics
The open access journal at the forefront of physics
Deutsche Physikalische Gesellschaft DPG | IOP Institute of Physics

Azimuthal asymmetry in collective electron dynamics in relativistically transparent laser–foil interactions

R J Gray[1], D A MacLellan[1], B Gonzalez-Izquierdo[1], H W Powell[1], D C Carroll[2], C D Murphy[3], L C Stockhausen[4], D R Rusby[1,2], G G Scott[1,2], R Wilson[1], N Booth[2], D R Symes[2], S J Hawkes[2], R Torres[4], M Borghesi[5], D Neely[1,2] and P McKenna[1]

[1] SUPA Department of Physics, University of Strathclyde, Glasgow G4 0NG, UK
[2] Central Laser Facility, STFC Rutherford Appleton Laboratory, Oxfordshire OX11 0QX, UK
[3] SUPA School of Physics and Astronomy, University of Edinburgh, Edinburgh EH9 3JZ, UK
[4] Centro de Láseres Pulsados (CLPU), M5 Parque Científico, E-37185 Salamanca, Spain
[5] Centre for Plasma Physics, Queens University Belfast, Belfast BT7 1NN, UK
E-mail: paul.mckenna@strath.ac.uk

Received 16 April 2014, revised 25 July 2014
Accepted for publication 19 August 2014
Published 23 September 2014
New Journal of Physics **16** (2014) 093027
doi:10.1088/1367-2630/16/9/093027

Abstract

Asymmetry in the collective dynamics of ponderomotively-driven electrons in the interaction of an ultraintense laser pulse with a relativistically transparent target is demonstrated experimentally. The 2D profile of the beam of accelerated electrons is shown to change from an ellipse aligned along the laser polarization direction in the case of limited transparency, to a double-lobe structure aligned perpendicular to it when a significant fraction of the laser pulse co-propagates with the electrons. The temporally-resolved dynamics of the interaction are investigated via particle-in-cell simulations. The results provide new insight into the collective response of charged particles to intense laser fields over an extended interaction volume, which is important for a wide range of applications, and in particular for the development of promising new ultraintense laser-driven ion acceleration mechanisms involving ultrathin target foils.

Keywords: laser-plasma interaction, ion acceleration, charged particle dynamics

1. Introduction

Understanding the collective response of charged particles to intense laser radiation is not only of fundamental interest, but is also important for the development of potentially compact laser-driven electron [1] and ion [2, 3] accelerators. It also underpins a range of other intense laser-plasma physics, including high energy x-ray generation (bremsstrahlung [4], synchrotron [5, 6] and betatron [7] production), high harmonic generation [8], high-field physics [9], and the production of intense magnetic fields [10]. The collective expulsion of electrons from regions of higher to lower field amplitude occurs due to the ponderomotive force, which arises from the inhomogeneity of the oscillating electromagnetic fields [11]. For a linearly polarized laser pulse with electric field amplitude $\mathbf{E} = E(z)\sin(\omega t)\hat{\mathbf{x}}$, travelling in the +z direction, the force exerted can be expressed as [12]:

$$\mathbf{f_p} = -\frac{e^2}{4\gamma m_e \omega^2}\frac{\partial}{\partial z}\left[E^2(z)[1-\cos(2\omega t)]\right]\hat{\mathbf{z}}, \tag{1}$$

where ω is the laser frequency, m_e is the electron mass and γ is the electron Lorentz factor. The first term is time-averaged and the second is a time-dependent component which drives longitudinal electron oscillations at twice the laser frequency (2ω) [12]. In a foil target, electrons are driven forward from the region of the critical density, n_c (beyond which the laser light cannot propagate), by the first component, with a 2ω oscillation induced by the second [12]. In the specific case of targets in which relativistic induced transparency (RIT) [13–15] occurs, the transmitted part of the laser pulse also ponderomotively drives a significant electron momentum in the perpendicular (radial) direction. RIT occurs in ultra-thin foils due to a combination of thermal expansion of the local target electron population and an increase in the critical density to γn_c due to the relativistic correction to m_e with increasing laser intensity. It can also occur if the laser longitudinal ponderomotive force decreases the target thickness to the order of the plasma skin depth [16, 17]. The former process is illustrated schematically in figure 1, which also shows the longitudinal propagation of a ponderomotively-driven local region of enhanced electron density ahead of the laser pulse [18]. Transparency changes the nature of the interaction from *surface-dominated* to *volumetric* [19], such that the collective electron response to the laser field continues over an extended distance. Understanding charged particle dynamics in the RIT regime is particularly important for the development of promising new ion acceleration mechanisms such as Break-Out Afterburner (BOA) [20, 21] and RIT-acceleration (RITA) [18], and for schemes for which it is detrimental, such as radiation pressure acceleration (RPA) [22–24] (which is most effective just before transparency occurs).

Whereas the beam of electrons expelled by an intense laser ponderomotive field is typically azimuthally symmetric in the case of a symmetric laser pulse intensity profile, in a recent theoretical study of BOA, Yin *et al* [20] report on 3D particle-in-cell (PIC) simulations which predict asymmetry in the collective response of electrons in thin foil targets undergoing RIT. An $m = 2$ (e.g. $\cos(2\theta)$, where θ is the angle between the electron radial momentum vector and the polarization axis) variation in the electron response to the laser ponderomotive force is predicted to lead to the formation of electron density lobes in the direction orthogonal to the laser polarization and propagation axes. Although signatures of an annular profile in BOA-ion acceleration have been reported [21, 25], to date the predicted azimuthal asymmetry in the electrons has not been measured directly.

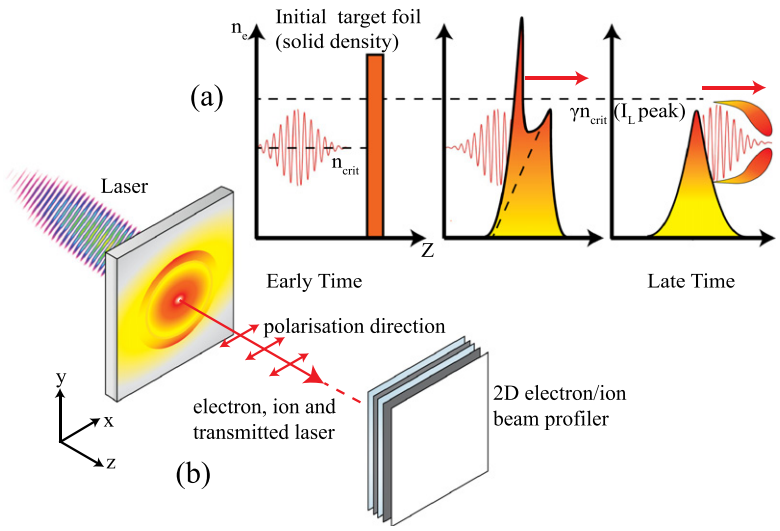

Figure 1. (a) Schematic illustrating the target electron density evolution and induced transparency. See main text for description. (b) Schematic showing the laser foil interaction and the position of the electron and proton spatial-intensity distribution detector.

In this paper, we report the first experimental demonstration of the asymmetry in the collective electron response to the radial ponderomotive force during RIT, as manifested in the formation of lobe structures in the spatial-intensity profile of the beam of electrons accelerated. The electron dynamics are shown, both experimentally and via PIC simulations, to be highly sensitive to the polarization of the drive laser pulse and the degree of transparency induced. The results highlight the potential to control the collective electron dynamics, the formation of resulting electrostatic fields, and hence the spatial-intensity profile of the beam of ions accelerated by these fields.

2. Experiment

The Astra–Gemini Ti:sapphire laser at the Rutherford Appleton Laboratory was used to produce pulses of 800 nm wavelength, λ, light, with typical duration, τ = 40 fs (full width at half maximum, FWHM), spot size of 3 μm (FWHM) and energy ~2 J (on-target, i.e. the energy after plasma mirrors and transport optics). For part of the study the laser pulse duration was varied in the range 40–160 fs by adding group velocity dispersion to the pulse via an acousto-optic modulator. A double plasma mirror arrangement enhanced the intensity contrast to $\sim 10^{11}$ and $\sim 10^{9}$, at 1 ns and 10 ps, respectively, prior to the peak of the pulse. The pulse was focused using an f/2 parabolic mirror, to a calculated peak intensity, I, of 7×10^{20} W cm^{-2} and incident along the target normal axis. A deformable mirror was employed prior to focusing to ensure a high quality focal spot. The laser light was linearly polarized, with the direction of polarization varied using a thin mica $\lambda/2$ wave-plate. The target was an aluminium foil, with thickness, L, varied in the range 10–800 nm. The energy of the portion of the laser light transmitted through the target (due to RIT) was monitored both by optical spectrometer measurements and by measuring the 2D spatial-intensity profile of the transmitted laser beam on a PTFE screen positioned behind the target, with a CCD camera. The energy transmission as measured by both

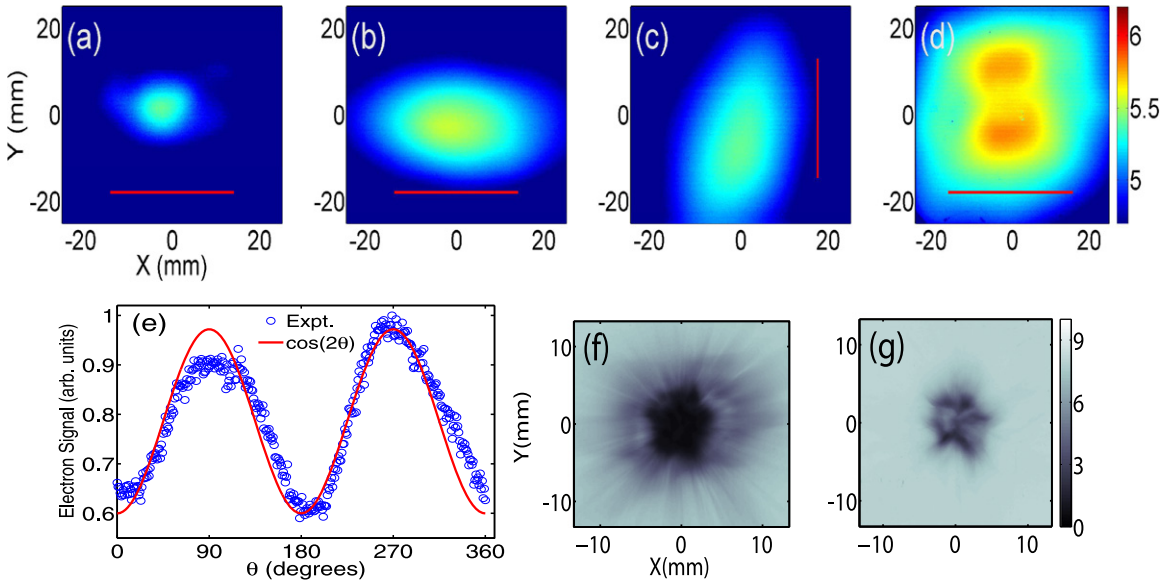

Figure 2. (a)–(d) 2D spatial-intensity distribution of the electron beam, for energy > 5 MeV, as measured with imaging plate, for: (a) $L = 800$ nm with polarization in the x-axis; (b) $L = 40$ nm with polarization in the x-axis; (c) $L = 40$ nm with polarization in the y-axis; and, (d) $L = 10$ nm with polarization in the x-axis. The laser polarization axis is shown as a red line. (e) Modulation in the electron signal as a function of θ (angle to the laser polarization) at 10 mm radius, corresponding to the lobe centre. (f)–(g) 2D spatial-intensity distribution of the proton beam, at ∼1 MeV (f) and ∼3 MeV (g), for $L = 10$ nm and polarization in the x-axis (the same laser shot as the electron distribution in (d)).

diagnostics was calibrated by comparing the recorded signal to the energy measured on a calorimeter on shots for which there was no target in the beam path.

The 2D spatial-intensity profile of the beam of electrons ponderomotively accelerated by the laser pulse was measured 3 cm downstream from the target using passive stacked layers of Fujifilm imaging plate (IP), interleaved with iron filters, and in separate shots, in real-time using a Kodak Lanex screen detector, with equivalent iron filtering. The 2D spatial-intensity and spectral profile of the beam of accelerated protons was simultaneously measured using stacked layers of radiochromic film, placed immediately in front of the IP stack, filtered for energy selection with thin layers of mylar and copper. The stacks were centred on the laser propagation (z-) axis, as illustrated in figure 1.

Figure 2 shows representative measurements of the spatial-intensity profiles of both the electron and proton beams, and exhibits the most salient features of the experimental results. The only laser pulse parameter varied for this data set is the direction of polarization ($\tau = 40$ fs and $I = 7 \times 10^{20}$ W cm^{-2}). For $L = 800$ nm, for which induced transparency does not occur, the electron beam is circular and relatively small. For $L = 40$ nm, a larger number of electrons are detected and the beam is highly elliptical, with the major axis parallel to the laser polarization. This is clear when comparing figures 2(b) and (c), for which the laser polarization vector is along the x- and y-axis, respectively. Similar polarization-sensitive electron beam ellipticity has been previously observed in laser-underdense plasma interactions [26] (but not with overdense targets) and indicates strong electron interaction with the laser electric field.

Figure 2(d) shows the corresponding case for polarization in x and a $L = 10$ nm target, for which a double-lobe structure, centred on the laser propagation axis and orientated in the axis perpendicular to the laser polarization, is measured. In figure 2(e) the electron signal at the radius corresponding to the peak of the lobes is plotted as a function of θ (angle with respect to the polarization axis). The variation in the distribution has a cos (2θ) dependence, which is in good agreement with the theoretical predictions of Yin *et al* [20]. The double-lobe structure in the electron density arises due to the plasma response to the propagating laser field. Although the radial ponderomotive force is axisymmetric, as described in reference [20] a cos (2θ) variation arises in the collective response of the electrons to the combined radial force and the laser E-field (the angular variation arising from a dot product in the momentum component terms).

We find that the double lobe structure is only measured for the thinnest target explored ($L = 10$ nm). Figures 2(f) and (g) shows the corresponding proton beam profile at two proton energies sampled. Generally we find that with decreasing target thickness the proton beam becomes more structured, with evidence of hollowing for $L = 10$–40 nm. The highest proton flux is typically measured off-axis, which is a signature of BOA-ion acceleration (see references: [21, 25]). At low proton energies radial spoke features are also clearly observed for $L = 10$ nm, and the prominence of this feature also decreases with increasing L. By considering the magnitude and evolution of the charge separation-induced electrostatic fields, as determined from numerical simulations discussed below, we calculate that the measured double-lobe electron distribution could give rise to proton lobes separated by ∼6 mm at the position of the RCF detector. The features observed in figure 2(g) are separated by about this scale, but a double-lobe structure is not clearly observed. The separation of the expected proton lobes will increase with the duration of the electrostatic field and hence the drive laser pulse. The theoretical study in which a double-lobe ion distribution is predicted was performed for laser pulses with $\tau > 150$ fs [20].

Figure 3(a) shows the measured percentage of laser light transmitted as a function of L. Only a few percent is transmitted for $L = 40$ nm, rising to ∼10 % for $L = 20$ nm and ∼30 % for $L = 10$ nm. The measured changes to the electron and proton beam profiles are thus shown to be correlated with the onset of RIT.

3. Simulations of the onset of RIT

To investigate this correlation in more detail, 2D3V simulations were performed using the fully relativistic electromagnetic PIC code EPOCH. Full 3D PIC simulations at the required spatial and temporal resolutions and solid density requires high performance computing resources much beyond those available for this study. However, 2D3V simulations enable core aspects of the collective effects governing RIT and the resulting electron dynamics to be explored. The simulation grid comprised a total of 7.2 million cells with ten particles per cell and a spatial resolution of 0.5 × 0.8 nm. The laser pulse had a Gaussian profile both temporally and spatially. The target consisted of two species, electrons and Al^{13+} ions at a density $n_e/n_{cr} = 447$. In order to resolve the Debye length the initial electron and ion temperatures were $T_e = 10$ keV and $T_i = 40$ eV, respectively. Simulations were performed as a function of laser polarization, target thickness (10, 20 and 40 nm), laser intensity (up to 6×10^{20} W cm^{-2}) and pulse duration ($\tau =$ 40–160 fs). The simulation plane is y-z and the laser is incident along target normal (z-axis) and propagates only 200 nm in vacuum before reaching the target front surface (laser light therefore reaches the target 1.5 fs after the start of the simulation, ensuring interaction with an initially solid density target).

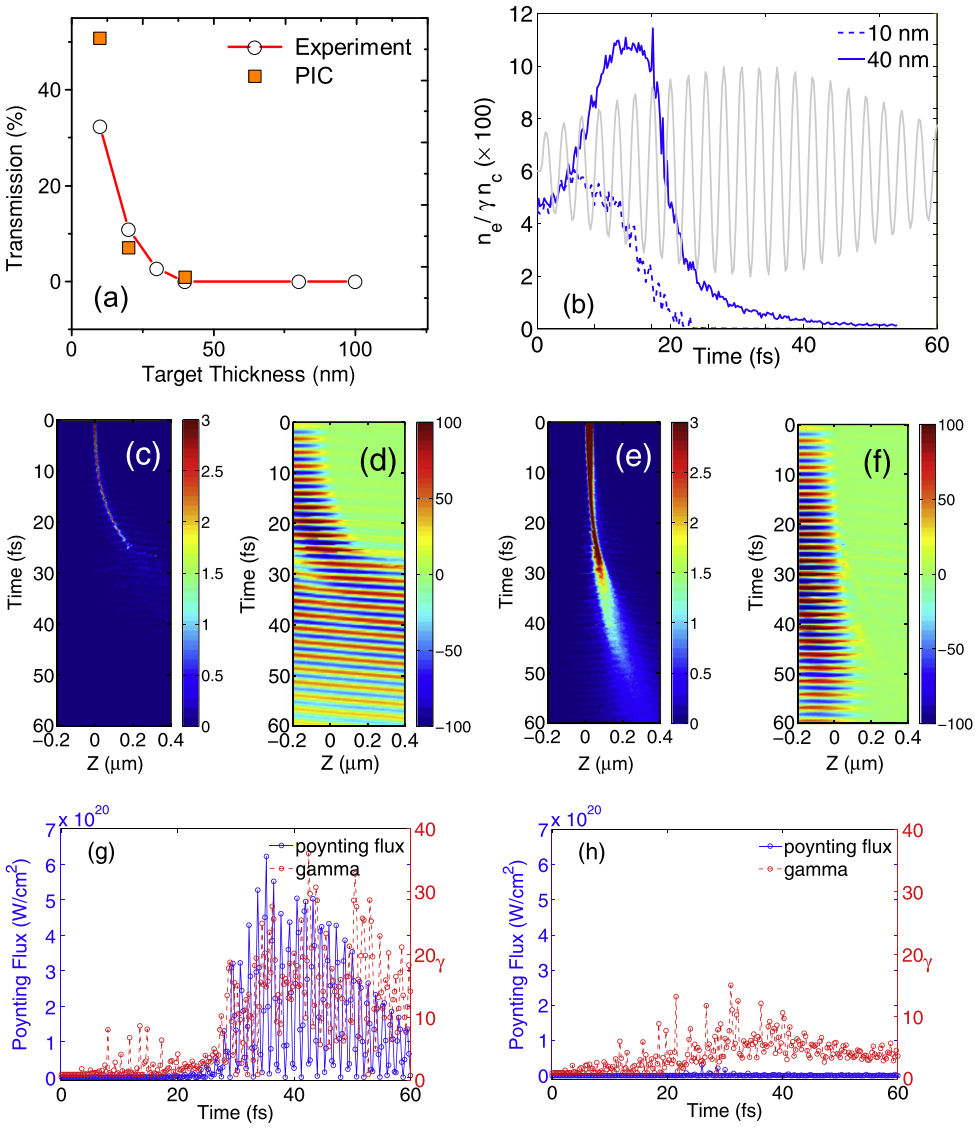

Figure 3. (a) Comparison between experiment and simulation results for the transmitted percentage of the laser pulse energy as a function of target thickness. (b) Evolution of the peak electron density in the PIC simulation (at any position across the evolving electron density profile) for $L = 10$ nm and 40 nm. The laser pulse temporal profile is shown in the background for reference. (c) Electron density (in units of $100n_e/n_c$) and (d) laser electric field (in units of TV m^{-1}) along the laser propagation (z) axis as a function of time, for $L = 10$ nm; (e) and (f) are the corresponding plots (same units) for $L = 40$ nm; (g) evolution of the laser Poynting flux and the electron Lorentz factor 600 nm from the target rear surface for $L = 10$ nm; (h) corresponding plots for $L = 40$ nm.

As shown in figure 3(a), the predicted onset of transparency is in good agreement with the experimental results, albeit that the percentage of transmitted light is higher than that measured for the 10 nm thick target case. Simulations for $L = 40$ nm exhibit minimal transparency. As shown in figure 3(b), for this case the peak electron density increases by more than a factor 2 in response to the laser ponderomotive drive, and decreases to γn_c only very late in the laser pulse

(which is included as a background plot). By contrast, for $L = 10$ nm significant transparency occurs as the peak density decreases to γn_c on the rising edge of the laser pulse. The temporal evolution of the electron density and the laser electric field along the laser propagation axis (y = 0) is shown in figures 3(c) and (d), respectively, for $L = 10$ nm, and in figures 3(e) and (f), respectively, for $L = 40$ nm. The effects of radiation pressure are observed in both cases, with the $L = 10$ nm target becoming transparent after 30 fs. The $L = 40$ nm case remains overdense throughout the simulation time.

The evolution of the electron Lorentz factor and the Poynting flux (which is a diagnostic of laser energy) at an example distance of 600 nm downstream from the initial rear surface of the target, are shown in figures 3(g) and (h), for $L = 10$ nm and 40 nm, respectively. For the $L = 10$ nm case transparency occurs after ~30 fs, and the Lorentz factor increases by more than a factor of two in response to the transmitted laser pulse. There is no appreciable increase in the electron Lorentz factor downstream for the $L = 40$ nm case. The results presented in figure 3 all involve polarization in the plane of the simulation box. These results confirm that for the parameters of the experiment, significant transparency occurs for $L = 10$ nm and that the propagated portion of the laser pulse continues to act on the accelerated electrons over an extended volume at the target rear.

To further confirm that the degree of RIT occurring defines the spatial-intensity distribution of the electron beam, we extended both the experiment and simulation study to investigate the sensitivity to the laser pulse duration, for fixed target thickness $L = 10$ nm. Figures 4(a)–(d) shows that the orientation of the major axis of the resulting elliptical electron beam (measured on the lanex screen) changes from being aligned perpendicular to the laser polarization for a $\tau = 40$ fs pulse to being parallel for $\tau = 160$ fs. Corresponding simulation results for the temporal evolution of the electron density and laser electric field along the laser propagation axis are shown in figures 4(e)–(h) for two example cases, $\tau = 80$ fs and 160 fs. The Poynting flux and Lorentz factor (as for the $\tau = 40$ fs results in figure 3(g)), are shown in figures 4(i) and (j), for $\tau = 80$ fs and 160 fs, respectively. In all cases the laser polarization vector is in the plane of the simulation. The simulations confirm that the degree of transparency decreases with increasing pulse duration, because of the decreasing peak laser intensity. These results, when considered together with those in figure 3, demonstrate that the orientation of the electron spatial-intensity distribution is sensitive to the degree of laser light transmission.

In the discussion so far, the onset of transparency is described in terms of the combined effect of the increasing electron Lorentz factor, on the rising edge of the laser pulse, coupled with the thermal expansion of electrons into vacuum resulting in a reduced peak electron density, such that laser pulse propagation can occur part way through the interaction [13, 14]. This physical picture is rigorously true for infinite plasmas. In the case of target thicknesses comparable to the plasma skin depth, the transparency conditions are modified due to additional effects such as the longitudinal ponderomotive force at the plasma interface [27]. Vshivkov *et al* [16] derive the conditions for relativistic transparency in a thin slab of overdense plasma as $a_o \gg \omega_p^2 L/2c\omega$, where ω and ω_p are the laser and plasma frequency, respectively, L is the target thickness and a_o is the light amplitude (equation (50) in reference [16]). For the parameters of the present experiment, this condition is satisfied only for $L < 20$ nm (with the terms on the right side equal to a_o for $L = 70$ nm). Thus our results are also in good agreement with the analytical model of RIT in thin plasma slabs [16]. We have also considered the role of light pressure compressing the electrons in the thin target such that the effective target width as seen by the laser becomes of the order of, or less than, the skin depth, as discussed in reference

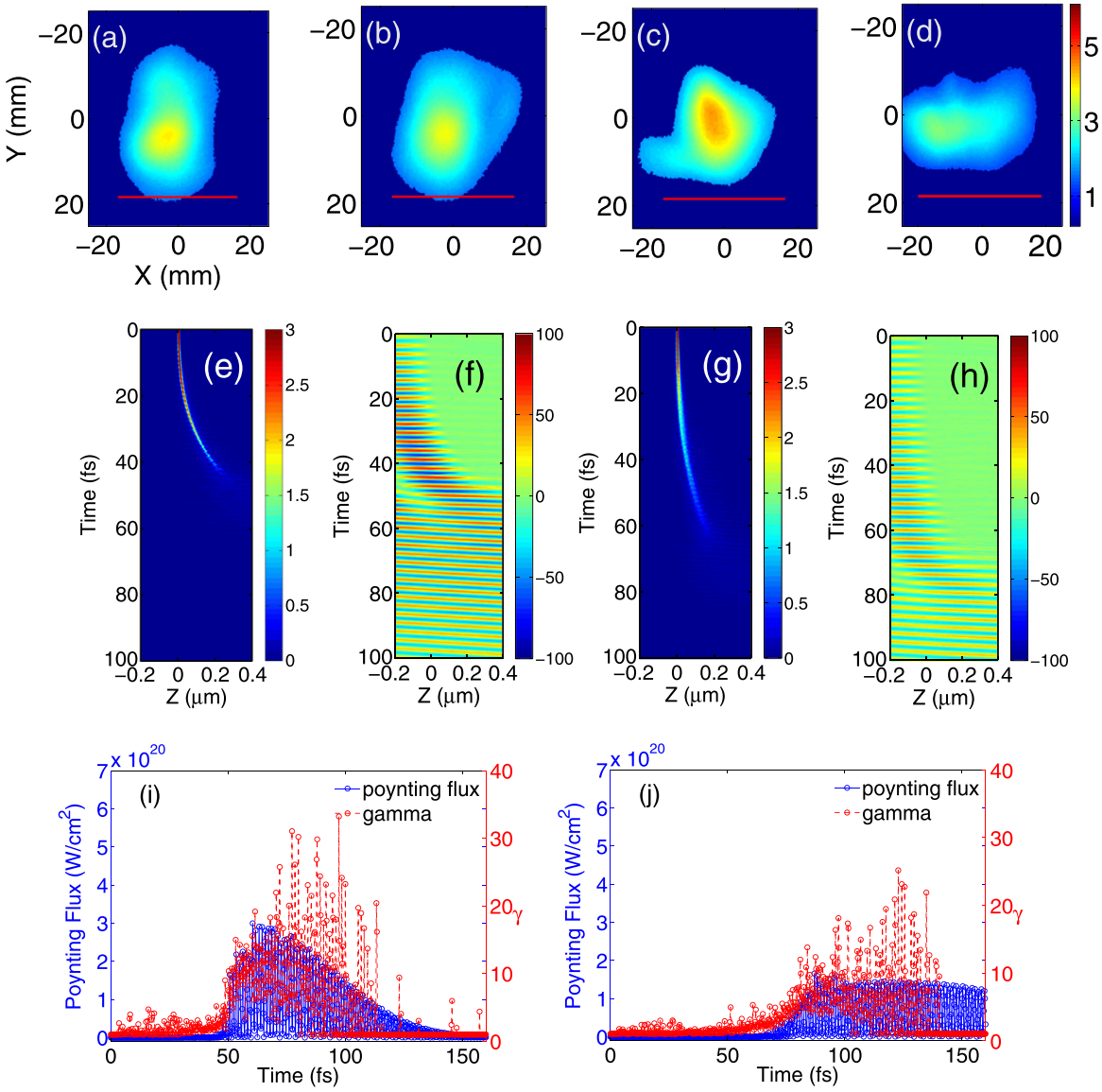

Figure 4. (a)–(d) Experiment results: 2D spatial-intensity distribution of the electron beam density (in arbitrary units) for energy > 5 MeV, as measured with a Lanex screen, for: (a) $\tau = 40$ fs; (b) $\tau = 80$ fs; (c) $\tau = 120$ fs, and (d) $\tau = 160$ fs. The laser is polarized along the x-axis in all four cases and the target thickness is 10 nm; (e)–(j): simulation results: (e) electron density (in units of $100n_e/n_c$) and (f) laser electric field (in units of TV m^{-1}) along the z-axis as a function of time, for a $\tau = 80$ fs pulse; (g) and (h) are the corresponding plots (same units) for a $\tau = 160$ fs pulse; (i) evolution of the laser Poynting flux and the electron Lorentz factor 600 nm downstream from the target rear surface for a $\tau = 80$ fs pulse; (j) corresponding plots for a $\tau = 160$ fs pulse.

[17]. Whereas this can contribute to inducing transparency in thin foils in the case of circularly polarized laser light, due to the constant light pressure and reduced electron heating, in the case of linear polarization and the other laser and target parameters considered here our simulations indicate that RIT occurs predominately through plasma expansion reducing the peak electron density.

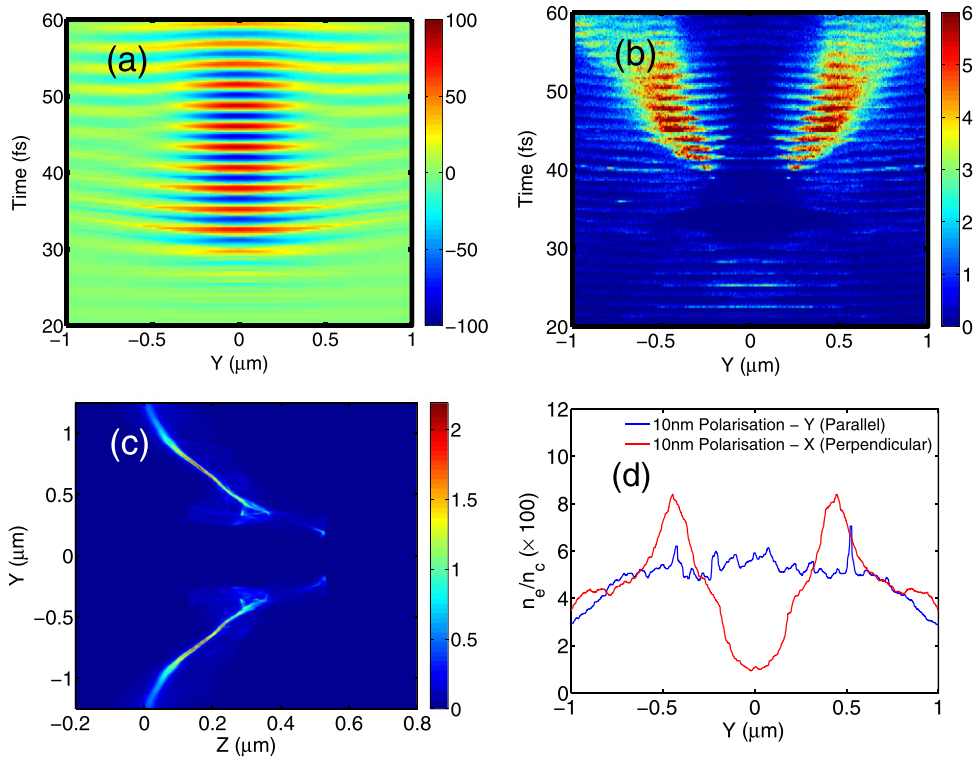

Figure 5. PIC simulation results showing the temporal evolution of (a) E_x, the laser E-field (in TV m^{-1}) and (b) the electron density (in units of n_e/n_c), along the y-axis, at 600 nm downstream from the rear surface of a $L = 10$ nm target; (c) example 2D profile of the electron density at 35 fs, just after RIT has occurred (in units of $100n_e/n_c$); (d) time-integrated electron density profile along the y-axis (at 600 nm from the rear surface) for the two laser polarization directions.

4. Modelling axial asymmetry in the plasma response to RIT

Detailed numerical investigation of the asymmetry in the collective electron response to the onset of transparency requires high resolution 3D simulations with an initially solid density target, which are computationally intensive and beyond the resources available in the present study. However, the 2D3V EPOCH code used employs a 2D simulation plane with 3 field and velocity components, which enables aspects of the asymmetry to be explored by comparing the 1D electron density profiles along the y-axis in simulation runs with the polarization parallel (y-polarized) and perpendicular (x-polarized) to the simulation plane.

In figure 5 we explore the electron response for the $L = 10$ nm case. Figures 5(a) and (b) show the temporally-resolved E-field of the transmitted laser light and the electron density, respectively, as measured 600 nm downstream from the target rear surface. The laser is polarized in the x-axis (i.e. perpendicular to the plane of the simulation), and, as before, $t = 0$ corresponds to the start of the simulation. Electrons ponderomotively driven forward (longitudinally) by the laser pulse are ejected first from the target and detected downstream after about 20 fs. This population is relatively small in number compared to the dense population which arrives later and as a result shows up as a relatively weak signal along the y = 0 axis in figure 5(b). Before the target undergoes RIT it is driven forward by laser radiation

pressure, to a maximum on-axis displacement of ~300 nm. After 30 fs the target is relativistically transparent and the reminder of the laser pulse is transmitted, as shown in figure 5(a). Figure 5(c) shows an example 2D profile of the target at 35 fs (just after RIT has occurred). The simulations reveal strong radial expulsion of the electrons due to the radial ponderomotive force of the transmitted laser light and a longitudinal oscillation of the electrons in response to the 2ω component of the ponderomotive force, which results in bunches of electrons being ejected forward towards the diagnostic point downstream. As shown in figure 5(b), the density distribution of the radially expelled electrons (detected 600 nm downstream after 40 fs) is modulated at 2ω.

Temporally integrated electron density profiles for the cases in which the distribution is sampled parallel and perpendicular to the laser polarization vector are compared in figure 5(d). The double-peak feature observed *perpendicular* to the laser polarization (x-polarized), which changes to a more uniform distribution for the *parallel* case (y-polarized), is qualitatively consistent with the experimental results in figure 2(d). A more detailed numerical study of the underlying physics and comparison with the annular dependence measured experimentally requires full 3D simulations and will be the subject of future work.

5. Summary

In summary, the collective dynamics of electrons in a relativistically transparent foil driven by a linearly polarized laser field is experimentally shown to exhibit a $\cos(2\theta)$ dependence, as manifested in a double lobe formation in the electron density distribution. A theoretical framework for 3D electron fluid ponderomotive dynamics during RIT is presented by Yin *et al* [20] and predicts the measured asymmetry as arising from the collective response of the electrons to the non-oscillating component of the radial ponderomotive force. The electron beam profile is further shown to be sensitive to the laser polarization direction and the percentage of the laser energy that is transmitted through the target. The degree of structure in the proton beam is also found to be correlated to the onset of transparency. A future experimental study with higher energy laser pulses, for which RIT is induced over a longer pulse duration, is required to investigate the interaction between the electron and ion dynamics in more detail.

Acknowledgements

We acknowledge the expert support of the staff at the Central Laser Facility of the Rutherford Appleton Laboratory and the use of the ARCHIE-WeST high performance computer. This work is supported by EPSRC (grant numbers EP/J003832/1, EP/L001357/1 and EP/K022415/1), LASERLAB-EUROPE (grant agreement n 284464, EC's Seventh Framework Programme) and sponsored by the Air Force Office of Scientific Research, Air Force Material Command, USAF (grant number FA8655–13-1–3008). LCS acknowledges LA^{3}NET, which is funded by the European Commission under Grant Agreement Number GA-ITN-2011-289191. The EPOCH code was developed under EPSRC grant EP/G054940/1. The research data associated with this paper will be available at the following link from January 2015: https://pure.strath.ac.uk/portal/en/persons/paul-mckenna(9094b0aa-58f7-4f06-b71c-86f3d322887d).html.

References

[1] Esarey E, Schroeder C B and Leemans W P 2009 *Rev. Mod. Phys.* **81** 1229
[2] Daido H, Nishiuchi M and Pirozhkov A S 2012 *Rep. Prog. Phys.* **75** 056401
[3] Macchi A, Borghesi M and Passoni M 2013 *Rev. Mod. Phys.* **85** 751
[4] Norreys P A *et al* 1999 *Phys. Plasmas* **6** 2150
[5] Kneip S *et al* 2010 *Nat. Phys.* **6** 980
[6] Rousse A *et al* 2004 *Phys. Rev. Lett.* **93** 135005
[7] Cipiccia S *et al* 2011 *Nat. Phys.* **7** 867
[8] Dromey B *et al* 2012 *Nat. Phys.* **8** 804
[9] Bell A R and Kirk J G 2008 *Phys. Rev. Lett.* **101** 200403
[10] Bell A R and Kingham R J 2003 *Phys. Rev. Lett.* **91** 035003
[11] Kibble T W B 1966 *Phys. Rev. Lett.* **16** 1054
[12] Kruer W L and Estabrook K 1985 *Phys. Fluids* **16** 430
[13] Kaw P and Dawson J 1970 *Phys. Fluids* **13** 472
[14] Akhiezer A I and Polovin R V 1956 *Sov. Phys.-JETP* **3** 696–705
[15] Guerin S *et al* 1996 *Phys. Plasmas* **3** 2693
[16] Vshivkov V A *et al* 1998 *Phys. Plasmas* **5** 2727
[17] Yu W *et al* 1999 *Phys. Rev.* E **59** 3583
[18] Sahai A A *et al* 2013 *Phys. Rev.* E **88** 043105
[19] Henig A *et al* 2009 *Phys. Rev. Lett.* **103** 045002
[20] Yin L *et al* 2011 *Phys. Rev. Lett.* **107** 045003
[21] Jung D *et al* 2013 *New J. Phys.* **15** 123035
[22] Esirkepov T *et al* 2004 *Phys. Rev. Lett.* **92** 175003
[23] Henig A *et al* 2009 *Phys. Rev. Lett.* **103** 245003
[24] Kar S *et al* 2012 *Phys. Rev. Lett.* **109** 185006
[25] Hegelich B M *et al* 2013 *New J. Phys.* **15** 085015
[26] Mangles S P D *et al* 2006 *Phys. Rev. Lett.* **96** 215001
[27] Cattani F *et al* 2000 *Phys. Rev.* E **62** 1234